

Model Fitting Using RANSAC for Surgical Tool Localization in 3-D Ultrasound Images

Marián Uherčík*, Jan Kybic, *Senior Member, IEEE*, Hervé Liebgott, and Christian Cachard

Abstract—Ultrasound guidance is used for many surgical interventions such as biopsy and electrode insertion. We present a method to localize a thin surgical tool such as a biopsy needle or a microelectrode in a 3-D ultrasound image. The proposed method starts with thresholding and model fitting using random sample consensus for robust localization of the axis. Subsequent local optimization refines its position. Two different tool image models are presented: one is simple and fast and the second uses learned *a priori* information about the tool's voxel intensities and the background. Finally, the tip of the tool is localized by finding an intensity drop along the axis. The simulation study shows that our algorithm can localize the tool at nearly real-time speed, even using a MATLAB implementation, with accuracy better than 1 mm. In an experimental comparison with several alternative localization methods, our method appears to be the fastest and the most robust one. We also show the results on real 3-D ultrasound data from a PVA cryogel phantom, turkey breast, and breast biopsy.

Index Terms—Electrode, localization, needle, 3-D ultrasound, randomized algorithm, random sample consensus (RANSAC), ultrasound guidance.

I. INTRODUCTION

IN SURGICAL practice, small instruments such as needles and electrodes are inserted into biological tissue. For example, in biopsy, tissue samples are taken from a particular region by means of a thin needle [1]. In prostate brachytherapy, small radioactive rods are inserted inside the tissue via a hollow shaft [2]. In breast cancer therapy, radioactive substance is injected near the tumor [3]. For neurological research, the

electrical activity of a specific group of neurons is recorded by a thin electrode [4]. In all these examples, it is important to localize the instruments for the determination of their precise position. The desired accuracy depends on the application: for needle biopsy, it is of the order of millimeters [5], and for electrode insertion, it is a submillimeter accuracy.

A stereotactic frame for instrument guidance was introduced in 1908 [6]. Medical imaging techniques (e.g., magnetic resonance imaging (MRI), computed tomography (CT), and ultrasound imaging) are now also used for guidance [7] in clinical practice; localization is mostly done visually by a human expert. We focus herein on ultrasound imaging, which is a widely available standard technique with real-time acquisition speed [8]. There are no known adverse health effects and the cost is relatively modest.

The task addressed in this study is to automatically determine a 3-D position of an elongated tool (needle or electrode) in biological tissue in an ultrasound image using a fast and robust algorithm. One application is to show or emphasize the 3-D location of a tool within ultrasound images and to automatically choose the most appropriate viewpoint or the imaging plane for 2-D visualization so that the clinician can check the location of the tool in the tissue. The localization information could also be used as initialization in an automatic guidance system during a surgical intervention.

Most tool localization methods in 3-D are based on parallel projections. A method of Ding *et al.* [9] detects the needle in 2-D parallel projection (for a given direction) using a volume rendering technique. A similar method of Aboofazeli *et al.* [10] can also detect curved needles. Both the methods find the 3-D location of the needle by projecting the needle back to the 3-D volume. Many approaches based on the Hough transform (HT) have been proposed for straight line detection. Zhou *et al.* used a randomized HT (RHT) [11] for straight-needle segmentation in thresholded 3-D ultrasound images. The RHT discretizes the parameter space and randomly samples pairs of 3-D voxels after thresholding, incrementing the appropriate accumulator bin. This is unlike the standard HT, which samples one point per iteration, incrementing a number of accumulator bins. Quick RHT (QRHT) [12] reduces the computational effort by doing the RHT only on coarse resolution volumes and subsequently refining the solution in the proximity. Okazawa *et al.* [13] generalized the HT for detection of curved needles in 2-D ultrasound images. Another method based on the generalized HT represents the tool as a Bézier curve [14], allowing the curved shape to be modeled. On a graphical processing unit (GPU), a real-time speed can be achieved. The idea of modeling the tool using Bézier curves can be also applied to a RHT.

Manuscript received July 30, 2009; revised January 28, 2010 and March 9, 2010; accepted March 14, 2010. Date of publication May 18, 2010; date of current version July 14, 2010. The work of M. Uherčík was supported by an European Commission Project under Grant MEST-CT-2005-021024 Wide Area Research Training in Health Engineering (WARTHE). The work of J. Kybic was supported by Czech Ministry of Education Project under Grant MSM6840770012. Asterisk indicates corresponding author.

*M. Uherčík is with the Department of Cybernetics, Faculty of Electrical Engineering, Center for Machine Perception (CMP), Czech Technical University in Prague, Prague 16627, Czech Republic, and also with the CREATIS-LRMN, Université de Lyon, INSA-Lyon, Université Lyon 1, Centre National de la Recherche Scientifique (CNRS) Unité Mixte de Recherche 5220, Institut National de la Santé et de la Recherche Médicale (INSERM) U630, France (e-mail: uhercik@cmp.felk.cvut.cz).

J. Kybic is with the Department of Cybernetics, Faculty of Electrical Engineering, Center for Machine Perception (CMP), Czech Technical University in Prague, Prague 16627, Czech Republic (e-mail: kybic@fel.cvut.cz).

H. Liebgott and C. Cachard are with the CREATIS-LRMN, Université de Lyon, Institut National des Sciences Appliquées (INSA)-Lyon, Université Lyon 1, Centre National de la Recherche Scientifique Unité Mixte de Recherche 5220, Institut National de la Santé et de la Recherche Médicale U630, France (e-mail: liebgott@creatis.insa-lyon.fr; christian.cachard@creatis.insa-lyon.fr).

Color versions of one or more of the figures in this paper are available online at <http://ieeexplore.ieee.org>.

Digital Object Identifier 10.1109/TBME.2010.2046416

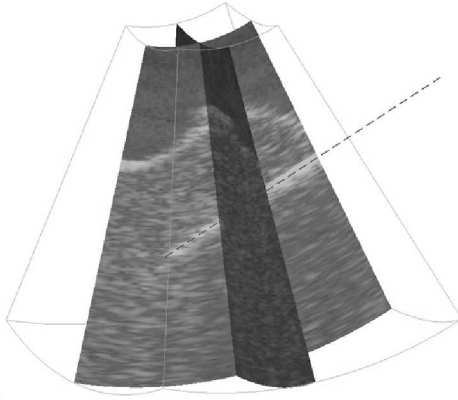


Fig. 1. Example of a 3-D ultrasound image of a PVA cryogel phantom in water. Inside the phantom there is a tungsten electrode. Two planar sections (one of them passing through the electrode axis) are shown in grayscale. The diagonal dashed line is the localization result. A thin wireframe shows the scanned volume boundaries.

Barva *et al.* [15] proposed to use the parallel integral projection (PIP) to localize straight cylindrical objects in 3-D images. This approach is based on the observation that a projection of a tool is minimized when the projection is performed along the tool's axis. The PIP is related to a generalized 3-D Radon transform (RT) [16]. It decomposes the search into a mesh-grid search over the two rotation angles and an exhaustive search in the projection plane. Additional PIP speedup can be achieved through a multiresolution approach and an early stopping [17]. Novotny *et al.* [18] proposed a method similar to the PIP derived from the generalized RT, achieving real-time speed by dividing the 3-D volume into smaller spherical regions and using a fast parallel implementation on a GPU. The general disadvantage of projection-based methods is their computational complexity and the lack of robustness when applied to the localization of very thin objects (1 mm or less in diameter) in a highly cluttered background (see experimental comparison in Section III). Hence, there is a need to find a new, more robust, and computationally efficient approach.

II. METHOD

The study presented herein is based on a model-fitting approach described by Barva [19]. Given a 3-D ultrasound image (see Fig. 1), our method is able to find the position and orientation of thin elongated objects such as electrodes or needles. With respect to the aforementioned projection-based methods (HT, RHT, or PIP), the presented method is designed to be faster, more robust to the presence of other high-intensity structures, and to allow more generally shaped models.

The algorithm is based on the following two assumptions.

- 1) *Assumption 1:* The intensity of the tool's voxels is higher than the surrounding tissue.
- 2) *Assumption 2:* The shape of the tool is a thin, long, and possibly curved cylinder.

The tool might be deformed during insertion and steering due to lateral forces [20]. Bending is typical for thin electrodes

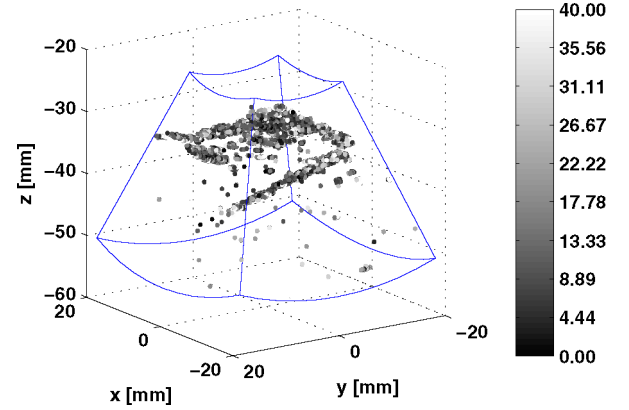


Fig. 2. 3-D ultrasound image from Fig. 1 after thresholding. Intensity values shown are normalized by the means of all voxels. A blue wireframe shows the volume boundaries.

(diameter around 0.3 mm). Biopsy needles are thicker (diameter around 1 mm), and therefore, remain straight.

Our goal is to localize the axis and the tip of the tool with submillimeter accuracy, which is sufficient for all intended applications. The task is challenging for several reasons: the diameter of the tool can be as small as the physical resolution of the ultrasound. The images contain a large amount of speckle noise, and some parts of the tissue can have a level of intensity similar to the tool. The proposed algorithm consists of four steps

- 1) Thresholding—the set of voxels to consider is reduced by thresholding using Assumption 1 (see Section II-A).
- 2) Axis localization—an approximate position of the tool's axis is estimated by a robust randomized search procedure random sample consensus (RANSAC) (see Section II-D).
- 3) Local optimization—a more accurate solution is found using local optimization (see Section II-E).
- 4) Tip localization—the endpoint of the tool is identified along the tool's axis (see Section II-F).

Steps 2 and 3 are based on a model describing the tool's shape and intensity in the image (see Section II-B and II-C).

A. Thresholding

A set of voxels with coordinates $\mathcal{X} \subseteq \mathbb{R}^3$ and intensities $I(\mathcal{X}) \subseteq \mathbb{R}$ is split by thresholding into two disjoint sets: \mathcal{X}_t (tool's voxels) and \mathcal{X}_b (background voxels)

$$\begin{aligned} \mathcal{X}_t &= \{\mathbf{x} \in \mathcal{X} : I(\mathbf{x}) \geq T_I\} \\ \mathcal{X}_b &= \mathcal{X} \setminus \mathcal{X}_t. \end{aligned} \quad (1)$$

As an example, a thresholded 3-D image \mathcal{X}_t from Fig. 1 is shown in Fig. 2. All subsequent processing uses only the subset \mathcal{X}_t in order to reduce the processing time.

The threshold T_I can be found by minimizing voxel classification error, assuming that labeled training data are available. Otherwise, the threshold is chosen empirically. Barva estimates the threshold as the 95% quantile of the input data by fitting a Gamma distribution [19], which seems to work in practice. This is based on the expectation that the proportion of voxels belonging to the tool is less than 5%. Note that the

resulting \mathcal{X}_t also contains some non-tool voxels (outliers), which will have to be filtered out later (see Section II-D).

B. Axis Model

The tool's axis is represented by a spatial parametric polynomial curve $a(t; \mathbf{H}) : \mathbb{R} \rightarrow \mathbb{R}^3$ of order $n - 1$

$$a(t; \mathbf{H}) = \underbrace{\begin{pmatrix} h_{11}, \dots, h_{1n} \\ h_{21}, \dots, h_{2n} \\ h_{31}, \dots, h_{3n} \end{pmatrix}}_{\mathbf{H}} \begin{pmatrix} 1 \\ t \\ \vdots \\ t^{n-1} \end{pmatrix}, \quad t \in \mathbb{R}. \quad (2)$$

We use $n = 2$ to model straight tools; polynomial curves of low order $n = 3$ can model bent tools (C-like shapes) and occasionally higher values of n might be also useful (S-like shapes for $n = 4$). The curve is determined by n control points $\mathbf{p}_i \in \mathbb{R}^3$, $i = 1, \dots, n$ through which it is required to pass. A principal direction \mathbf{k}_0 is determined by fitting a straight line to points \mathbf{p}_i . We then choose the parameters t_i according to a projection onto this line

$$t_i = \frac{(\mathbf{p}_i - \mathbf{p}_1)\mathbf{k}_0}{\|\mathbf{k}_0\|}. \quad (3)$$

Finally, the matrix \mathbf{H} is found by solving the following system of $3n$ linear equations

$$a(t_i, \mathbf{H}) = \mathbf{p}_i, \quad \forall i : 1 \leq i \leq n \quad (4)$$

after substituting $a(t_i, \mathbf{H})$ from (2).

C. Tool's Models

Two models (AxShp, IntDstr) are proposed for the tool's shape and intensity in 3-D ultrasound images to be used in steps 2 and 3 of the algorithm (see Section II). Each model consists of a function $q(\mathbf{x}; \mathbf{H}) \in \{1, 0\}$ classifying each voxel \mathbf{x} with intensity $I(\mathbf{x})$ as either a tool ($q = 1$), or a background ($q = 0$); and a cost function $C(\mathcal{X}_{\text{inl}}; \mathbf{H})$ quantifying how well the model parameters \mathbf{H} fit a set of voxel observations \mathcal{X}_{inl} consistent with the model (inliers).

The tool's shape, i.e., curve parameters \mathbf{H} , are first estimated roughly by maximizing the number of tool's voxels (inliers \mathcal{X}_{inl}) as determined using the function $q(\mathbf{x}; \mathbf{H})$ by RANSAC (see Section II-D). Afterwards, the solution is refined by local optimization of the cost function $C(\hat{\mathcal{X}}_{\text{inl}}; \mathbf{H})$ on the best set of estimated inliers $\hat{\mathcal{X}}_{\text{inl}}$ (see Section II-E).

1) *Axshp Model*: This simple model evaluates only the distances of the points $\mathbf{x} \in \mathcal{X}_t$ to the curve $a(t; \mathbf{H})$. It does not use any *a priori* information on the intensity values and no training is needed. The classification function $q(\mathbf{x})$ uses a distance $d(\mathbf{x}; \mathbf{H})$ of the point \mathbf{x} to the curve $a(t, \mathbf{H})$

$$q_{\text{AxShp}}(\mathbf{x}; \mathbf{H}) = \begin{cases} 1, & \text{if } d(\mathbf{x}; \mathbf{H}) \leq \tau \\ 0, & \text{otherwise.} \end{cases} \quad (5)$$

The threshold τ is set as the expected radius of the tool in the image. The model's cost $C(\mathbf{H})$ is the sum of the squared

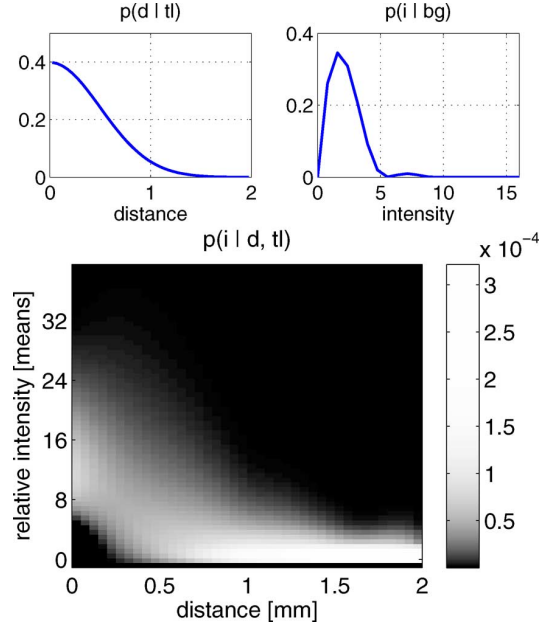


Fig. 3. Examples of empirically learned distributions $p(i|d, tl)$, $p(d|tl)$ and $p(i|bg)$ used in the IntDstr model. The distributions were estimated from a training set of nine images of an electrode in a PVA cryogel phantom.

distances to the axis

$$C_{\text{AxShp}}(\mathcal{X}_{\text{inl}}; \mathbf{H}) = \sum_{\mathbf{x} \in \mathcal{X}_{\text{inl}}} d(\mathbf{x}; \mathbf{H})^2. \quad (6)$$

The cost function is smooth (unlike $\sum q_{\text{AxShp}}(\mathbf{x}; \mathbf{H})$, used in [19]), which is important for the local optimization later.

As the true point-to-curve distance would be prohibitively expensive to calculate, the following approximation is used:

$$d(\mathbf{x}; \mathbf{H}) = \|\mathbf{x} - a(t; \mathbf{H})\|$$

$$\text{with } t = \frac{(\mathbf{x} - \mathbf{p}_1)\mathbf{k}_0}{\|\mathbf{k}_0\|} \quad (7)$$

which is good as long as the curvature of $a(t; \mathbf{H})$ is small.

2) *IntDstr Model*: This model is based on an estimated likelihood $p(d, i|c)$ of observing a voxel \mathbf{x} with an intensity $i = I(\mathbf{x})$ at distance d (7) from the axis, given its class c (tool “tl” or background “bg”). The classification function q is chosen as a likelihood comparison test

$$q_{\text{IntDstr}}(\mathbf{x}; \mathbf{H}) = \begin{cases} 1, & \text{if } p(d, i|tl) \geq p(d, i|bg) \\ 0, & \text{otherwise.} \end{cases} \quad (8)$$

The model's cost function $C(\mathbf{H})$ is a log-likelihood of observing the set of inliers \mathcal{X}_{inl} , given a tool position and assuming that voxel observations are independent

$$C_{\text{IntDstr}}(\mathcal{X}_{\text{inl}}; \mathbf{H}) = \sum_{\mathbf{x} \in \mathcal{X}_{\text{inl}}} -\log p(d, i|tl). \quad (9)$$

The dependence of $p(d, i|c)$ on \mathbf{H} is implicit through d (7).

The likelihood $p(d, i|tl)$ for tool's voxels is decomposed as follows:

$$p(d, i|tl) = p(i|d, tl) p(d|tl)$$

$$\text{with } p(d|tl) = N_{0, \sigma}^+(d) \quad (10)$$

Input:
 \mathcal{X}_t — thresholded voxels.
 q — classification function from AxShp or IntDstr models.

Output:
 $\hat{\mathcal{X}}_{\text{inl}}$ — estimated inliers.
 $\hat{\mathbf{H}}$ — estimated curve parameters.
 $\hat{\mathcal{P}}$ — control points on the estimated curve.

```

j ← 1; J ← Jmax;
while j ≤ J do
  1) Randomly select a subset  $\mathcal{P} \subset \mathcal{X}_t$ ,  $|\mathcal{P}| = n$  and
  compute  $\kappa(\mathcal{S}_j)$ . If  $\kappa(\mathcal{P}) \leq \kappa_{\text{max}}$ , then continue;
  otherwise repeat step 1;
  2) Compute matrix  $\mathbf{H}$  from control points  $\mathcal{P}$  (2–4);
  3) Estimate a set of inliers  $\mathcal{X}_{\text{inl}}$  (12);
  4) Update the best-so-far model:
    if  $|\mathcal{X}_{\text{inl}}| > |\hat{\mathcal{X}}_{\text{inl}}|$  then
      a)  $\hat{\mathbf{H}} := \mathbf{H}$ ;  $\hat{\mathcal{P}} := \mathcal{P}$ ;  $\hat{\mathcal{X}}_{\text{inl}} := \mathcal{X}_{\text{inl}}$ ;
      b) Update the number of iterations  $J$  (13);
    else j ← j + 1;
end

```

Algorithm 1: RANSAC procedure to robustly estimate parameters of the tool's axis from the thresholded points \mathcal{X}_t .

where $N_{0,\sigma}^+(d)$ is the positive part of a normal distribution with zero mean and variance σ (for simplicity) corresponding to the expected radius of the tool in the image. The background intensity $p(d, i | \text{bg})$ is assumed to be spatially independent, i.e.,

$$p(d, i | \text{bg}) = p(i | \text{bg}). \quad (11)$$

Both $p(i | d, \text{tl})$ and $p(i | \text{bg})$ are estimated from a training set of images with a known ground truth. The tool's voxels are first collected into m uniformly sized bins $b_j = [j\Delta d; (j+1)\Delta d]$ according to a distance d from the tool. The distributions of voxel intensities $p(i | \text{bg})$ and $p(i | d \in b_j, \text{tl})$ for $j = 0, \dots, m-1$ are modeled as Gamma distributions $\Gamma_{k_{\text{bg}}, \theta_{\text{bg}}}$ and Γ_{k_j, θ_j} , respectively. The Gamma distribution is sufficiently general to approximate the real distribution well, and it was successfully used for ultrasound images in [19] and [21]. The parameters $\sigma, k_{\text{bg}}, \theta_{\text{bg}}, k_j$, and θ_j are determined as maximum likelihood estimates [22]. Examples of learned distributions are shown in Fig. 3.

D. RANSAC Procedure

The RANSAC procedure was introduced by Fischler and Bolles [23] to solve the problem of robust estimation of model parameters, given a set of input samples with a large number of outliers. In our case, the input of the RANSAC procedure is a set of thresholded voxels \mathcal{X}_t and a classification function q_{AxShp} or q_{IntDstr} . The RANSAC outputs are the identified curve parameters $\hat{\mathbf{H}}$ and a corresponding set of points $\hat{\mathcal{X}}_{\text{inl}}$ consistent with this model.

In each RANSAC iteration (see Algorithm 1), first a sample consisting of a set $\mathcal{P} = \{\mathbf{p}_i, i = 1, \dots, n\}$ of n distinct points \mathbf{p}_i is randomly selected from \mathcal{X}_t (see step 1 of Algorithm 1). To quickly filter out sets leading to excessively curved axes (which would not lead to good solutions anyway), samples with

$\kappa(\mathcal{P}) > \kappa_{\text{max}}$ are rejected, where the pseudo-curvature $\kappa(\mathcal{P})$ is defined as the maximum orthogonal distance between one of the control points \mathbf{p}_i and a straight line $l(\mathcal{P})$ fitted to all n points \mathcal{P} , and κ_{max} is set to maximum expected deformation. The coefficient matrix \mathbf{H} is calculated from \mathcal{P} as described in Section II-B (see step 2) and a set of inliers is estimated (see step 3)

$$\mathcal{X}_{\text{inl}}(\mathbf{H}) = \{\mathbf{x} \in \mathcal{X}_t \mid q(\mathbf{x}; \mathbf{H}) = 1\}. \quad (12)$$

The best curve parameters $\hat{\mathbf{H}}$ found so far, based on the number of estimated inliers $|\mathcal{X}_{\text{inl}}|$ (see step 5), are stored together with the corresponding control points $\hat{\mathcal{P}}$ and a set of consistent points $\hat{\mathcal{X}}_{\text{inl}}$.

The number of iterations J to perform is initially set to J_{max} (typically a few hundred) and it is then adaptively updated [see step 4(b)] whenever a better model is found [23], [24]

$$J = \frac{\ln(1 - \eta)}{\ln(1 - \zeta^n)}, \quad \text{with } \zeta = \frac{|\mathcal{X}_{\text{inl}}|}{|\mathcal{X}_t|} \quad (13)$$

where ζ estimates the inlier ratio and η is a user-defined parameter; a desired probability that n inliers are selected at least once during J iterations, i.e., that RANSAC succeeds.

E. Local Optimization

The RANSAC procedure gives a robust approximation of the axis position. However, its accuracy is limited, since the model parameters $\hat{\mathbf{H}}$ are computed only from n control points. Therefore, a more accurate solution \mathbf{H}^* is found based on the complete estimated set of inliers $\hat{\mathcal{X}}_{\text{inl}}$ by minimizing the cost function $C(\hat{\mathcal{X}}_{\text{inl}}; \mathbf{H})$ (see Section II-C).

Instead of optimizing the coefficients \mathbf{H} directly, we optimize the position of the control points \mathcal{P} because it is numerically more stable. Moreover, it is enough to vary the point positions in a direction perpendicular to the axis.

First, the local coordinate system \mathbf{K} is calculated from the set $\hat{\mathcal{X}}_{\text{inl}}$ by principal component analysis, where \mathbf{K} consists of principal directions $\mathbf{k}_0, \mathbf{k}_1, \mathbf{k}_2$, in the decreasing order of corresponding eigenvalue magnitudes ($|\lambda_0| \geq |\lambda_1| \geq |\lambda_2|$).¹ The position of the control points along the \mathbf{k}_0 are not important for the shape of the curve. To reduce the redundancy of the parameterization, the control points $\hat{\mathcal{P}}$ are reparameterized using a matrix \mathbf{E} with dimensions $2 \times n$

$$\underbrace{[\mathbf{p}_1, \dots, \mathbf{p}_n]}_{\mathcal{P}(\mathbf{E})} = \underbrace{[\hat{\mathbf{p}}_1, \dots, \hat{\mathbf{p}}_n]}_{\hat{\mathcal{P}}} + [\mathbf{k}_1 \quad \mathbf{k}_2] \mathbf{E}. \quad (14)$$

The curve parameters $\mathbf{H}(\mathbf{E})$ are calculated from control points $\mathcal{P}(\mathbf{E})$ by solving the linear system (4), as described in Section II-B. The cost function C from Section II-C is optimized with respect to variable \mathbf{E}

$$\mathbf{H}^* = \arg \min_{\mathbf{E}} C(\hat{\mathcal{X}}_{\text{inl}}; \mathbf{H}(\mathbf{E})). \quad (15)$$

¹In Section II-B, a principal direction \mathbf{k}_0 is also calculated but only from the n control points.

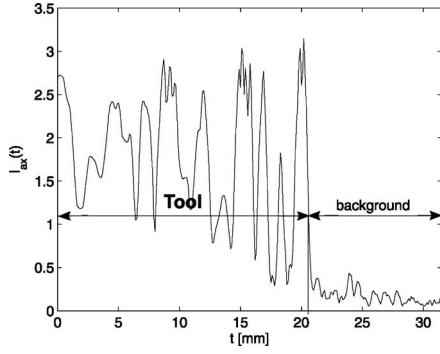


Fig. 4. Axis tip localization example. Typical voxel intensity along the tool's axis. A threshold is determined based on training data, and short segments are removed. A large intensity variation is observed in the tool area.

The optimization is done using a derivative-free Nelder–Mead downhill simplex method [25] with an initial estimate $\mathbf{E} = \mathbf{0}$.

F. Tip Localization

Once the axis location has been found, the values of all voxels along the axis are considered and the tip of the tool is identified as a significant drop by the method of Barva *et al.* [15] (see Fig. 4), consisting of thresholding with *a priori* determined value T and mathematical morphology operations to skip small breaks caused by speckle noise in the ultrasound image. The tool is usually inserted from outside so that only one tip is present in the image. The threshold T is calculated from two *a priori* estimated distributions: probability of the tool voxel $P(\text{tl} | I)$ and the background voxel $P(\text{bg} | I)$, respectively, given the voxel intensity I . The threshold T is set such that $P(\text{tl} | T) = P(\text{bg} | T)$. Then probability distributions are estimated on training data with known location of the tool.

G. Implementation Details

We use a straight line [$n = 2$ in (2)] or a quadratic curve [$n = 3$ in (2)] for cases, where tool is expected to be bent (see Section III-A2 and III-B2). The desired probability for successful RANSAC termination was set to $\eta = 0.99$. Increasing η , further improves the accuracy by 5%–15% at the expense of an increased number of iterations. Local optimization usually terminates in not more than 40 steps, taking about 26% of the total time. The majority of the memory was used for storing the 3-D volume (90 MB for 3-D data of size $53 \times 71 \times 3100$ voxels). The RANSAC localization algorithm takes the thresholded points as input, which is only a small fraction of the full set of points; therefore, the additional memory requirements for the RANSAC are negligible.

All algorithms were implemented in MATLAB² on a standard PC with Intel Core 2 processor at 1.83 GHz. Further speedup should be possible by rewriting them in a compiled language such as C++. Our preliminary experiments with implementation of the RANSAC method in C++ show that the speed-up is at least by a factor of three.

²The MathWorks, Natick, MA.

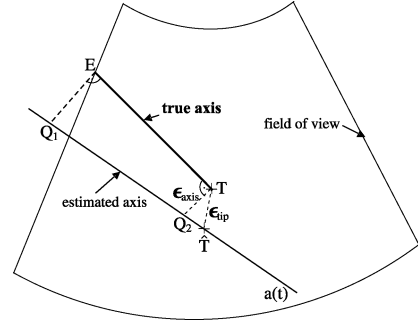


Fig. 5. Illustration of the axis and endpoint accuracy evaluation. The ground-truth tool's position is determined by an intercept point E and a tool's tip T . It is compared with an axis $a(t)$ and a tip \hat{T} estimated by the proposed method.

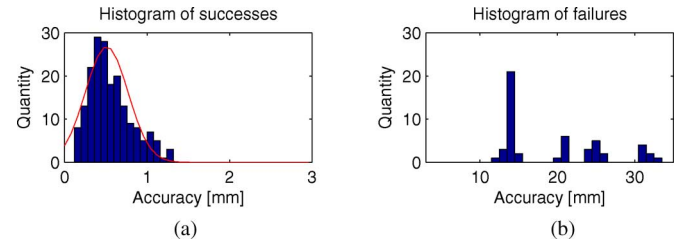


Fig. 6. Example of histograms of axis accuracies measured for AxShp model fitting on PVA cryogel phantom. (a) For successful runs ($\epsilon_{\text{axis}} < 3$ mm) with a fitted normal distribution shown as red line. (b) For failures ($\epsilon_{\text{axis}} \geq 3$ mm).

H. Accuracy Assessment

Two measures are used to quantify the accuracy of the proposed method [19]. Tip localization accuracy is

$$\epsilon_{\text{tip}} = \|T - \hat{T}\| \quad (16)$$

where T is the true tool's tip and \hat{T} is an estimated tip. Axis localization accuracy ϵ_{axis} is given by

$$\epsilon_{\text{axis}} = \max \{\|E - Q_1\|, \|T - Q_2\|\} \quad (17)$$

where E is the true intercept point, and Q_1 and Q_2 are the orthogonal projections of E and T on $a(t)$ with respect to the true axis (see Fig. 5). Angular error, which is also sometimes used to measure localization accuracy, is related to ϵ_{axis} and the tool's length.

The result is considered a failure when $\epsilon_{\text{axis}} \geq 3$ mm or $\epsilon_{\text{tip}} \geq 3$ mm. The number of failures is reported separately and accuracy is evaluated only on successful runs. Example of sample histograms for accuracy ϵ_{axis} in Fig. 6(a) for successful runs shows that accuracies approximately follow a normal distribution, while for failures [see Fig. 6(b)], the errors are significantly higher. We have performed statistical significance tests for comparison of the proposed method to the other methods. Specifically, we do a *t*-test [26] with a significance level of 5% ($p = 0.05$) for accuracy ϵ_{axis} and also for the number of failures. The experiments are repeated many times (with different random seeds) so that enough measurements are accumulated for the distribution of the number of failures to be approximately normal and the *t*-test to be applicable.

TABLE I
OVERVIEW OF DATASETS USED FOR EXPERIMENTS

Data	Resolution	Section	Results
Simulation	$53 \times 71 \times 3100$	III-A1	Table II
PVA phantom	$53 \times 71 \times 3100$	III-B1	Table III
PVA phantom	$53 \times 71 \times 3100$	III-B1	Table IV
Turkey Breast	$273 \times 376 \times 196$	III-B2	Table V
Breast biopsy	$273 \times 383 \times 208$	III-B3	Table VI
Breast biopsy	$273 \times 383 \times 208$	III-B3	Table VII

III. RESULTS

The results of the localization algorithm are presented on simulated data, on real ultrasound data of a phantom with an inserted tool, and on real data from a breast biopsy. The true tool's position in simulated data is known; for real ultrasound data, it was found as a mean of the estimates of ten human observers. The mean variability for human observers was less than 0.4 mm. All 3-D visualizations shown in this section were made in Paraview [27].

The proposed method is compared to other projection-based localization methods (see also Section I) such as the RHT [11], the QRHT [12], the PIP method [15], the multiresolution PIP (MR-PIP) method [17], and the fast MR-PIP (Fast MR-PIP) method [17]. The number of bins for the RHT and the QRHT is set to 36 and 16, respectively, for each of four dimensions. In the PIP method, an angular resolution of 1° and spatial resolution of 0.2 mm is used; its multiresolution version [17], (MR-PIP) uses three resolution levels, and its fast variant (Fast MR-PIP) stops the optimization at the second resolution level. All algorithms use the same method for tip localization (see Section II-F).

In the experiments described in the following, the randomized algorithms were repeated 30 times (on each test data set) with different random seeds. We report the mean time for each method. For the RANSAC method, we also report the mean number of iterations because the time complexity of the RANSAC depends directly on it. We give an overview of all data sets in Table I. The first three data sets were computed as the envelope of the acquired RF signals with high axial resolution. To study the effect of axial resolution on the localization accuracy, we have performed the localization with the envelope volumes downsampled $10\times$ (in the axial direction); the axis localization accuracy was not significantly affected. The last three datasets were acquired using a different 3-D scanner as standard B-mode images.

A. Simulation Study

A data set mimicking breast tissue was created using the software package Field II [28]. The simulator parameters were set to imitate an ultrasound scanner Voluson 530D³ operating at a central frequency of 7.5 MHz. Background scatterers were distributed according to a smoothed real 3-D ultrasound image of a breast in order to obtain a realistic inhomogeneous background. A signal corresponding to a 0.6-mm-diameter tool (radius 0.3 mm) with metal-like acoustic parameters was

³GE Healthcare, U.K.

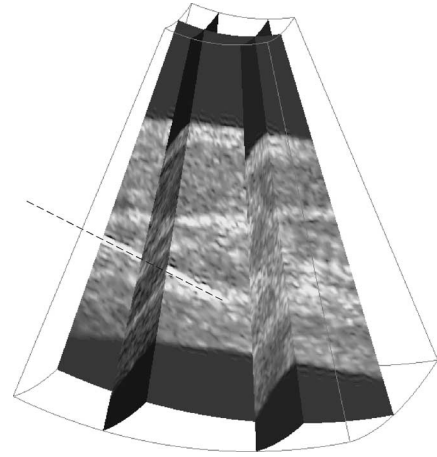


Fig. 7. Simulated ultrasound data using Field II with a tool and inhomogeneous background. A 2-D slice of a 3-D volume with the tool is selected. The estimated tool (marked by a dashed line) is oriented diagonally entering the volume from the left side.

TABLE II
AXIS ACCURACY, TIP ACCURACY, PERCENTAGE OF FAILURES, AND ELAPSED TIME FOR SIMULATED DATA WITH VARYING TOOL POSITIONS FOR DIFFERENT LOCALIZATION ALGORITHMS FOR THE SYNTHETIC INHOMOGENEOUS BACKGROUND CASE

Simulated data	Axis acc. [mm]	Tip acc. [mm]	Fails [%]	Time [s]
RNS+AxShp	0.14 ± 0.09	0.46 ± 0.50	0%	0.54
RNS+IntDstr	0.12 ± 0.08	0.48 ± 0.62	0%	2.22
RHT	0.38 ± 0.28	0.62 ± 0.59	2%	1.82
QRHT	1.41 ± 0.81	1.42 ± 0.99	28%	1.11
PIP	0.28 ± 0.12	0.53 ± 0.35	5%	69.1
MR-PIP	0.27 ± 0.13	0.45 ± 0.76	11%	29.4
Fast MR-PIP	0.56 ± 0.24	0.85 ± 0.62	11%	12.1

created by using highly reflecting scatterers. The background field and the tool field were summed in the RF signal domain, and a 3-D envelope image was calculated. This is equivalent to adding the tool as scatterers, but is faster when many datasets are created with the same background. An example volume of $53 \times 71 \times 3100$ voxels is shown in Fig. 7.

Parameter learning was performed on a training set of simulated data sets with varying tool locations, distinct from the testing set. The threshold T_I was set to maximize the inlier ratio (see Section II-A) to approximately 11 times the mean intensity. The threshold τ was set to 0.6 mm, which was the tool's observed radius.

1) *Tool Location*: Nine training and 19 testing datasets were prepared with varying depths and orientations of the straight tool with respect to the probe. The mean inlier ratio in the testing data was 30% and the mean number of RANSAC iterations was 60. The results (see Table II) show that the proposed methods (RANSAC with local optimization) are among the fastest and have the best repeatability (smallest standard deviation). The number of failures is nearly zero for the RANSAC, RHT, and PIP methods. However, the PIP method is very slow. It can be accelerated (MR-PIP methods), but the robustness is then reduced. There is a statistically significant difference (t -test, $p = 0.05$) between RANSAC and RHT axis accuracy, but not

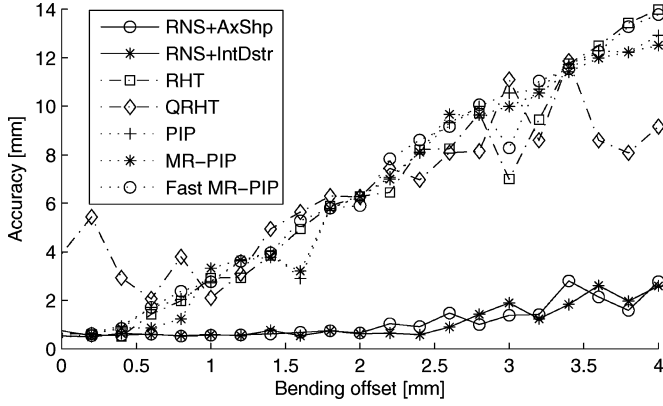


Fig. 8. Axis accuracy $\varepsilon_{\text{axis}}$ for varying tool offsets (bending) in simulated data. Failures were not discarded.

between the AxShp and IntDstr results. The RANSAC with the simple AxShp model is the fastest and should be chosen for this type of data.

2) *Tool Deformation*: The robustness of the tested methods with respect to tool deformation was evaluated on 21 test datasets. We used parameters learned in the previous experiment. The tool's axis was modeled by a quadratic ($n = 3$) polynomial curve, and the shape was controlled by bending the tool's tip. The tip bending offset varied between 0 (straight axis) and 4.0 mm for the total length of 20 mm. The results in Fig. 8 demonstrate that the axis localization error $\varepsilon_{\text{axis}}$ (we are not discarding failures in this case) for the RHT and the QRHT increases when applied to the data with a deformed tool. The performance of the proposed method does not deteriorate, because it represents the tool's axis as a polynomial curve.

3) *Signal-to-Noise Ratio*: The robustness of the tested methods with respect to noise was evaluated for data with varying tool's intensities with respect to the background. The SNR was defined as

$$\text{SNR} = \frac{\text{mean}[I(x_{\text{el}})]}{\text{mean}[I(x_{\text{bg}})]} \quad (18)$$

where x_{el} are voxels whose distance from the true axis is less than a tool's radius; the remaining voxels are considered as background x_{bg} . The percentage of failures is reported in Fig. 9 for SNR between 1.0 and 2.0—for higher SNR, all methods localized the tool perfectly, and for lower SNR, none of the methods found it. A group of nine training and 19 testing data sets were used for each SNR level. Note that the fastest method, RANSAC + AxShp, has about the same number of failures as the RHT. The RANSAC + IntDstr model is the most robust method.

B. Experiments on Real Data

1) *Polyvinyl Alcohol (PVA) Cryogel Phantom*: To mimic a biological tissue with a highly reflecting inclusion, a PVA cryogel phantom [29] with size 50 mm × 50 mm × 50 mm was created. Inside the phantom, there was a thin straight tungsten electrode 150 μm in diameter and 20 mm long. The phantom was scanned eight times from different directions by Voluson

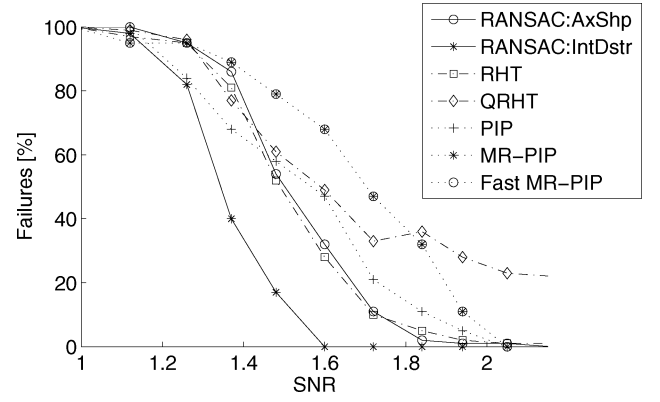


Fig. 9. Failure rate for varying SNR (tool contrast) on simulated data.

TABLE III
AXIS ACCURACY, TIP ACCURACY, THE PERCENTAGE OF FAILURES, AND ELAPSED TIME FOR EXPERIMENTS ON PVA CRYOGEL PHANTOM DATA FOR THE SMALL ROI

PVA phantom data	Axis acc. [mm]	Tip acc. [mm]	Fails [%]	Time [s]
RNS+AxShp	0.47 ± 0.31	0.46 ± 0.26	1%	0.66
RNS+IntDstr	0.91 ± 0.54	0.40 ± 0.32	0%	2.62
RHT	0.91 ± 0.44	0.80 ± 0.40	4%	2.13
QRHT	1.44 ± 0.75	0.99 ± 0.60	13%	2.19
PIP	0.33 ± 0.14	0.60 ± 0.21	25%	1268
MR-PIP	0.50 ± 0.31	0.80 ± 0.18	25%	342.1
Fast MR-PIP	0.33 ± 0.14	0.77 ± 0.25	25%	113.4

TABLE IV
AXIS ACCURACY, TIP ACCURACY, THE PERCENTAGE OF FAILURES, AND ELAPSED TIME FOR EXPERIMENTS ON PVA CRYOGEL PHANTOM DATA FOR THE FULL VOLUME

PVA phantom data	Axis acc. [mm]	Tip acc. [mm]	Fails [%]	Time [s]
RNS+AxShp	0.56 ± 0.27	0.64 ± 0.27	29%	5.67
RNS+IntDstr	0.55 ± 0.28	0.66 ± 0.31	14%	7.90
RHT	0.74 ± 0.33	0.98 ± 0.45	88%	3.81
QRHT	1.52 ± 0.67	0.63 ± 0.03	97%	2.07
PIP	0.34 ± 0.12	0.58 ± 0.12	50%	5615
MR-PIP	0.29 ± 0.12	0.45 ± 0.02	50%	1528
Fast MR-PIP	0.91 ± 0.25	0.62 ± 0.16	75%	537.2

530D ultrasound scanner with a 3-D probe operating at a central frequency of 7.5 MHz. The axial resolution was approximately 0.4 mm and the lateral resolution was 1 mm. The size of acquired volumes was $53 \times 71 \times 3100$ voxels.

All localization algorithms were tested in two variants: 1) we selected a small region of interest (ROI) with the electrode and 2) on full volume, which also contains the high-intensity phantom boundary. The results of the first experiment are shown in Table III. There is no statistically significant difference (t -test, $p = 0.05$) in the number of failures between the RANSAC and RHT methods. The mean inlier ratio was 20% and the number of RANSAC iterations was between 100 and 200. However, for the second experiment on the full volume in Table IV, the percentage of failures is statistically significantly smaller for the RANSAC than for the RHT and QRHT methods. The mean inlier ratio was only 5% and the number of RANSAC iterations

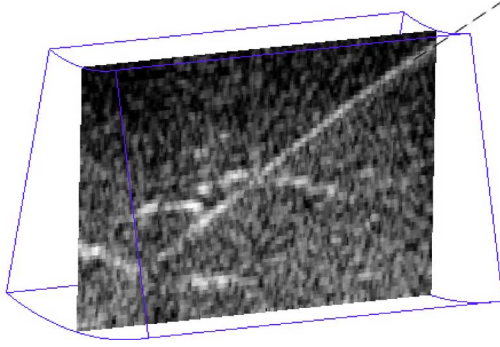


Fig. 10. Slice of a 3-D data of turkey breast with a needle. A 2-D slice of a 3-D volume with the needle is selected. The estimated tool (marked by a dashed line) is oriented diagonally entering the volume from the top-right side.

TABLE V

AXIS ACCURACY, TIP ACCURACY, PERCENTAGE OF FAILURES, AND ELAPSED TIME FOR ULTRASOUND DATA SHOWING A NEEDLE IN A TURKEY BREAST

Turkey breast	Axis acc. [mm]	Tip acc. [mm]	Fails [%]	Time [s]
RNS+AxShp	0.10 ± 0.05	0.19 ± 0.10	18%	2.24
RNS+IntDstr	0.09 ± 0.05	0.15 ± 0.07	16%	4.78
RHT	0.21 ± 0.11	0.13 ± 0.04	74%	1.74
QRHT	1.19 ± 0.14	1.37 ± 0.08	78%	1.37
PIP	N.A.	N.A.	100%	N.A.
MR-PIP	N.A.	N.A.	100%	N.A.
Fast MR-PIP	N.A.	N.A.	100%	N.A.

increased to 1000–2000. Therefore, the total time for RANSAC also increased.

The proposed RANSAC-based methods are very robust, especially using the IntDstr model, unlike the RHT, QRHT, and PIP methods, which are fooled by the presence of the phantom boundary in the 3-D volume. The PIP is the most accurate method, followed by RANSAC. An example of a localization result can be seen in Fig. 1. The AxShp model fitting is the fastest method, but using the model IntDstr is more robust to the presence of outliers.

2) *Experiments on Turkey Breast*: We acquired three datasets of turkey breasts with a 27-gauge needle (0.41 mm) inserted. The 3-D ultrasound images are $273 \times 376 \times 196$ voxels. The central frequency of the 3-D probe RSP6-16 RS varied between 10 and 18 MHz; so, the needle's appearance was different in each data set. Therefore, we had to train on each dataset separately. To make training and testing data distinct, we trained on different parts of the image than the part tested. The needle in the breast tissue was deformed in various ways; the maximal bending offset of the tool varied between 0.6 and 1.8 mm. The tool's length in the ROI was between 8 and 14 mm.

We selected a ROI containing the needle as well as some high-intensity structures (see Fig. 10). The results are shown in Table V. The mean inlier ratio was 16% and the number of RANSAC iterations was between 700 and 1000. There is a statistically significant difference (t -test, $p = 0.05$) between the number of failures for the RANSAC methods and RHT. The RANSAC has the lowest number of failures but longer process-

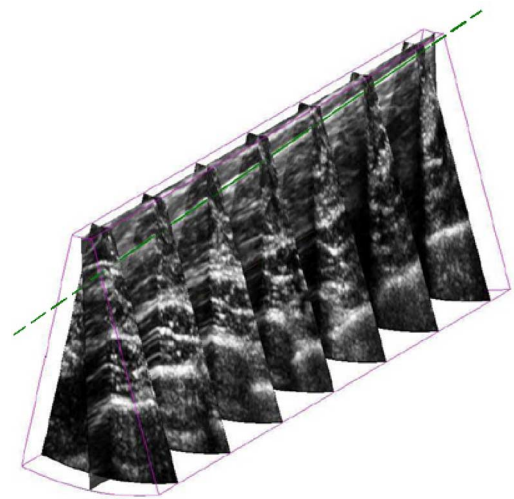


Fig. 11. 3-D view of data from breast biopsy. The boundary geometry of 3-D data is marked as a wireframe. There is one planar section of the data with a needle in the upper part and seven perpendicular planar sections. The dashed line shows the estimated needle direction.

TABLE VI

AXIS ACCURACY, TIP ACCURACY, PERCENTAGE OF FAILURES, AND ELAPSED TIME FOR BIOPSY ULTRASOUND DATA WITH A 19-GAUGE NEEDLE

Biopsy data	Axis acc. [mm]	Failures [%]	Time [s]
RNS+AxShp	0.20 ± 0.11	33%	0.64
RNS+IntDstr	0.17 ± 0.12	33%	2.29
RHT	0.52 ± 0.57	33%	4.31
QRHT	1.75 ± 0.47	79%	1.88
PIP	0.15 ± 0.0	67%	619
MR-PIP	N.A.	100%	198
Fast MR-PIP	N.A.	100%	28

ing time compared to other methods. We can observe here that RHT often fails on this data, probably because of bent needles, while the proposed methods are successful. The PIP methods all fail on this data.

3) *Experiments on a Breast Biopsy*: The usability of the proposed method on clinical data is demonstrated on real ultrasound datasets from a breast biopsy acquired by a 3-D U.S. scanner GE Voluson E8 with a 12-MHz probe (see Fig. 11). We acquired the three data sets with a mostly straight 19-gauge needle (1.092-mm outer diameter) and one data set with a 26-gauge needle. The 3-D ultrasound images are $273 \times 383 \times 208$ voxels.

The ROI was determined containing the needle as well as some various reflecting artifacts. The tip of the needle was located outside of the scanned volume area for three of the datasets; therefore, the tip localization measure was not applicable here. The axis accuracy and the time elapsed for the different methods are shown in Table VI. The last data set contains a thin needle that has a different appearance from the earlier group. We trained and tested on distinct parts of the volume. The results are reported in Table VII. In this case, tip localization accuracy was also evaluated because the electrode tip is visible.

The data used in this experiment are very challenging; therefore, all methods have a relatively high failure rate. Nevertheless, the RANSAC-based methods are the fastest, most robust, and

TABLE VII
AXIS ACCURACY, TIP ACCURACY, PERCENTAGE OF FAILURES, AND ELAPSED
TIME FOR BIOPSY ULTRASOUND DATA WITH A 27-GAUGE NEEDLE

Biopsy data	Axis acc. [mm]	Tip acc. [mm]	Fails [%]	Time [s]
RNS+AxShp	0.25 ± 0.10	0.97 ± 0.25	0%	1.66
RNS+IntDstr	0.24 ± 0.08	1.08 ± 0.49	0%	3.80
RHT	0.35 ± 0.26	0.87 ± 0.48	50%	2.67
QRHT	N.A.	N.A.	100%	2.5
PIP	N.A.	N.A.	100%	113
MR-PIP	N.A.	N.A.	100%	37.0
Fast MR-PIP	N.A.	N.A.	100%	6.5

most accurate. The PIP is also accurate but less robust and two orders of magnitude slower. RHT is as robust as RANSAC with speed similar to the IntDstr model but with worse accuracy.

IV. CONCLUSION

We proposed a method for fast and robust tool localization from 3-D ultrasound images based on the RANSAC, local optimization, and model fitting using one simple and one more complicated model. The simpler AxShp model is very fast and easy to implement and works well in most cases. The more complex IntDstr model can take advantage of the learned shape and intensity of the tool and the background, and works better in difficult low-SNR situations, but is several times slower.

The proposed RANSAC + AxShp method needs less than 1 s in MATLAB, which is approximately the time needed for an acquisition of one 3-D volume. A real-time implementation in a compiled language seems to be perfectly possible; we estimate a throughput of 3–5 fps on a single processor system. Earlier studies [14], [18] showed the feasibility of projection-based methods implemented on a GPU. RANSAC is also suitable for a parallel implementation. The accuracy is better than 1 mm, which is enough for all potential applications—visualization, localization, and guidance. The proposed method could be used for initialization of the tracking of the tool in a sequence of 3-D ultrasound volumes.

Our experimental results show that the methods proposed here are superior to all other methods tested. They are mostly as robust and fast as the RHT method while being more accurate, and as accurate as the PIP method while being about two orders of magnitude faster. The proposed methods are also more robust to low tool contrast and tool bending. We have shown that the methods can be successfully applied to real ultrasound data.

Further extensions include using additional features to distinguish the tool from the background, using *a priori* information about tool location, and parallelizing the algorithm for increased speed.

ACKNOWLEDGMENT

The authors would like to thank D. Buckton and C. Perrey from GE Medical Systems for providing the 3-D ultrasound breast biopsy and turkey breast data.

REFERENCES

- [1] A. Abati and A. Simsir, “Breast fine needle aspiration biopsy: Prevailing recommendations and contemporary practices,” *Clin. Lab. Med.*, vol. 25, no. 4, pp. 631–654, Dec. 2005.
- [2] G. S. Merrick, W. M. Butler, K. E. Wallner, R. W. Galbreath, and E. Adamovich, “Monotherapeutic brachytherapy for clinically organ-confined prostate cancer,” *W. V. Med. J.*, vol. 101, no. 4, pp. 168–171, Aug. 2005.
- [3] K. Kern, “Sentinel lymph node mapping in breast cancer using subareolar injection of blue dye,” *J. Amer. College Surg.*, vol. 189, no. 6, pp. 539–545, Dec. 1999.
- [4] R. L. Alterman, D. Sterio, A. Beric, and P. J. Kelly, “Microelectrode recording during posteroventral pallidotomy: Impact on target selection and complications,” *Neurosurgery*, vol. 44, no. 2, pp. 315–321, Feb. 1999.
- [5] N. Abolhassani, R. Patel, and M. Moallem, “Needle insertion into soft tissue: A survey,” *Med. Eng. Phys.*, vol. 29, no. 4, pp. 413–431, 2007.
- [6] V. Horsley and R. H. Clarke, “The structure and functions of the cerebellum examined by a new method,” *Brain*, vol. 31, pp. 45–124, 1908.
- [7] T. M. Peters, “Image-guidance for surgical procedures,” *Phys. Med. Biol.*, vol. 51, no. 14, pp. R505–R540, 2006.
- [8] J. W. Cannon, J. A. Stoll, and I. S. Salgo, “Real time 3-dimensional ultrasound for guiding surgical tasks,” *Comput. Aided Surg.*, vol. 8, pp. 82–90, 2003.
- [9] M. Ding, Z. Wei, L. Gardi, D. B. Downey, and A. Fenster, “Needle and seed segmentation in intra-operative 3D ultrasound-guided prostate brachytherapy,” *Ultrasonics*, vol. 44, no. 1, pp. 331–336, 2006.
- [10] M. Aboofazeli, P. Abolmaesumi, P. Mousavi, and G. Fichtinger, “A new scheme for curved needle segmentation in three-dimensional ultrasound images,” in *Proc. IEEE Int. Symp. Biomed. Imag.: From Nano to Macro*, Jun. 2009, pp. 1067–1070.
- [11] H. Zhou, W. Qiu, M. Ding, and S. Zhang, “Automatic needle segmentation in 3D ultrasound images using 3D improved Hough transform,” *Proc. SPIE Med. Imag. Parallel Process Images, Optim. Techn. (MIPPR)*, 2008, pp. 691821–1–691821–9. Available: http://spie.org/x648.html?product_id=749339.
- [12] W. Qiu, M. Ding, and M. Yuchi, “Needle segmentation using 3D quick randomized Hough transform,” *Proc. SPIE Intell. Netw. Intell. Syst. (ICNIS)*, pp. 449–452, 2008.
- [13] S. H. Okazawa, R. Ebrahimi, J. Chuang, R. N. Rohling, and S. E. Salcudean, “Methods for segmenting curved needles in ultrasound images,” *Med. Image Anal.*, vol. 10, no. 3, pp. 330–342, Jun. 2006.
- [14] H. Neshat and R. Patel, “Real-time parametric curved needle segmentation in 3D ultrasound images,” in *Proc. 2nd IEEE RAS & EMBS Int. Conf. Biomed. Robot. Biomechatronics*, 2008, pp. 670–675.
- [15] M. Barva, M. Uherčík, J.-M. Mari, J. Kybic, J.-R. Duhamel, H. Liebgott, V. Hlaváč, and C. Cachard, “Parallel Integral Projection transform for straight electrode localization in 3-D ultrasound images,” *IEEE Trans. Ultrasonics, Ferroelectr., Freq. Control*, vol. 55, no. 7, pp. 1559–1569, Jul. 2008.
- [16] S. Helgason, *The Radon Transform*, 2nd ed. New York: Birkhauser Boston, MA, 1999.
- [17] M. Uherčík, J. Kybic, H. Liebgott, and C. Cachard, “Multi-resolution parallel integral projection for fast localization of a straight electrode in 3d ultrasound images,” in *Proc. IEEE Int. Symp. Biomed. Imag.*, May 2008, pp. 33–36.
- [18] P. M. Novotny, J. A. Stoll, N. V. Vasilyev, P. J. del Nido, P. E. Dupont, and R. D. Howe, “GPU based real-time instrument tracking with three dimensional ultrasound,” *Med. Image Anal.*, vol. 11, no. 5, pp. 458–64, 2007.
- [19] M. Barva, “Localization of surgical instruments in 3D ultrasound images,” PhD thesis CTU–CMP–2007–12, Center for Machine Perception, K13133 FEE Czech Tech. Univ., Prague, Czech Republic, Jun. 2007.
- [20] S. P. Dimaio and S. E. Salcudean, “Needle insertion modeling and simulation,” *IEEE Trans. Robot. Autom.*, vol. 19, no. 5, pp. 2098–2105, Oct. 2003.
- [21] Z. Tao, C. C. Jaffe, and H. Tagare, “Tunnelling descent: A new algorithm for active contour segmentation of ultrasound images,” in *Proc. IPMI*, 2003, pp. 246–257.
- [22] S. C. Choi and R. Wette, “Maximum likelihood estimation of the parameters of the gamma distribution and their bias,” *Technometrics*, vol. 11, no. 4, pp. 683–690, Nov. 1969.
- [23] M. A. Fischler and R. C. Bolles, “Random sample consensus: A paradigm for model fitting with applications to image analysis and automated cartography,” *Commun. ACM*, vol. 24, no. 6, pp. 381–395, Jun. 1981.

- [24] P. H. S. Torr, A. Zisserman, and S. J. Maybank, "Robust detection of degenerate configurations while estimating the fundamental matrix," *Comput. Vis. Image Understanding*, vol. 71, no. 3, pp. 312–333, 1998.
- [25] J. A. Nelder and R. Mead, "A simplex method for function minimization," *Comput. J.*, vol. 7, pp. 308–313, 1965.
- [26] R. A. Fisher, *Statistical Methods for Research Workers*. Edinburgh, U.K.: Oliver & Boyd, 1970.
- [27] A. Henderson, *ParaView Guide*. Clifton Park, NY: Kitware Inc., 2007.
- [28] J. A. Jensen, "Field: A program for simulating ultrasound systems," in *Medical and Biological Engineering and Computing*, vol. 34. New York: Springer-Verlag, 1996, pp. 351–353.
- [29] J. Fromageau, E. Brusseau, D. Vray, G. Gimenez, and P. Delachartre, "Characterization of PVA cryogel for intravascular ultrasound elasticity imaging," *IEEE Trans. Ultrason., Ferroelectr., Freq. Control*, vol. 50, no. 10, pp. 1318–1324, Oct. 2003.



Marián Uherčík was born in Slovakia, in 1981. He received an Mgr. (M.Sc.) degree in informatics from the Faculty of Mathematics, Physics and Informatics, Comenius University, in Bratislava, Slovak Republic, in 2005. Currently, he is working toward the Ph.D. degree at the Center for Machine Perception, Faculty of Electrical Engineering, Czech Technical University, Prague, Czech Republic, and at the Center for Research and Applied Imaging and Signal Processing (CREATIS), Institut National des Sciences Appliquées (INSA), Lyon, France.

His research interests include medical applications and ultrasound imaging.



Jan Kybic (SM'08) was born in Prague, Czech Republic, in 1974. He received a Bc. (B.Sc.) and Ing. (M.Sc.) degrees (Hons.) from the Czech Technical University, Prague, in 1996 and 1998, respectively, and the Ph.D. degree in biomedical image processing from Ecole Polytechnique Fédérale de Lausanne (EPFL), Lausanne, Switzerland, in 2001 for his thesis on elastic image registration using parametric deformation models.

From October 2002 to February 2003, he was a Postdoctoral Research Fellow at Institut National de Recherche en Informatique et Automatique (INRIA), Sophia-Antipolis, France. Since 2003, he has been a Research Fellow in the Center for Machine Perception, Czech Technical University. His research interests include signal and image processing, medical imaging, image registration, splines and wavelets, inverse problems, elastography, computer vision, numerical methods, algorithm theory, and control theory.

Dr. Kybic is an Associate Editor of IEEE TRANSACTIONS ON MEDICAL IMAGING.



Hervé Liebgott received the M.Sc. degree in electrical engineering and the M.Sc. degree in acoustics, both in 2002, and the Ph.D. degree in acoustics, in 2005, all from the Institut National des Sciences Appliquées (INSA), Lyon, France.

Since 2002, he has been with the Medical Imaging Research Center (CREATIS), Université de Lyon, where he is engaged in the Ultrasonic Imaging Team. He is currently an Associate Professor at Université Claude Bernard Lyon 1, Villeurbanne, France, where he teaches in Génie Electrique et Informatique Industrielle (GEII), Institut Universitaire de Technologie (IUT). His research has been concerned with medical ultrasound. He is engaged in research on beam forming techniques for ultrasound imaging in order to facilitate their processing. The processing methods that are investigated are motion estimation for tissue elasticity imaging by ultrasound (elastography), motion estimation for echocardiography, and detection of highly echogenic objects in 3-D ultrasound data volumes.



Christian Cachard received the Ph.D. degree in acoustics from the Institut National des Sciences Appliquées (INSA), Lyon, France, in 1988 with special focus on acoustic signal processing for underwater acoustics.

He is currently a Professor in the Electrical Department, Technical Institute, Université Claude Bernard Lyon 1, Villeurbanne, France. Since he joined the research laboratory Medical Imaging Research Center (CREATIS), Université de Lyon, he has been engaged in the research on ultrasound medical imaging, ultrasound contrast agent imaging, ultrasound radio frequency processing, and microtools localization in 3-D ultrasound data.